Nanotechnology 28.40 (2017): 405705

DOI: http://dx.doi.org/10.1088/1361-6528/aa8505

Tunable plasmonic resonance of gallium nanoparticles by thermal oxidation at low temperatures

S. Catalán-Gómez[1]*, A. Redondo-Cubero[1], F.J. Palomares[2], F. Nucciarelli[1], J.L. Pau[1]

[1]*Grupo de Electrónica y Semiconductores, Departamento de Física Aplicada, Universidad Autónoma de Madrid, Cantoblanco, E-28049 Madrid (Spain).*

[2] *Instituto de Ciencia de Materiales de Madrid, CSIC, Cantoblanco, E-28049 Madrid (Spain).*

Corresponding author: sergio.catalan@uam.es

Abstract:

The effect of the oxidation of gallium nanoparticles (Ga NPs) on their plasmonic properties is investigated. Discrete dipole approximation has been used to study the wavelength of the out-of-plane localized surface plasmon resonance (LSPR) in hemispherical Ga NPs, deposited on silicon substrates, with oxide shell (Ga_2O_3) of different thickness. Thermal oxidation treatments, varying temperature and time, were carried out in order to increase experimentally the Ga_2O_3 shell thickness in the NPs. The optical, structural and chemical properties of the oxidized NPs have been studied by spectroscopic ellipsometry, scanning electron microscopy, grazing incidence X-ray diffraction and X-ray photoelectron spectroscopy. A clear redshift of the peak wavelength is observed, barely affecting the intensity of the plasmon resonance. A controllable increase of the Ga_2O_3 thickness as a consequence of the thermal annealing is achieved. In addition, simulations together with ellipsometry results have been used to determine the oxidation rate, whose kinetics is governed by a logarithmic dependence. These results support the tunable properties of the plasmon resonance wavelength in Ga NPs by thermal oxidation at low temperatures without significant reduction of the plasmon resonance intensity.

Keywords: Gallium, plasmonics, nanoparticles, ellipsometry, oxidation

1. Introduction

Plasmonics have attracted a great deal of attention in the last decades[1]. Its principle is based on the excitation of free electrons (plasmons) in metals, which enables the confinement of the electric field near the surface of metals. When electrons are confined in nanostructures, this phenomenon produces localized surface plasmon resonances (LSPRs) that can be used in many applications, including biosensing[2,3], plasmonic waveguiding[4,5] and optoelectronic devices with enhanced emission/absorption[6,7].

Metallic nanoparticles (NPs) are excellent systems to produce LSPRs due to their size, geometry and electric properties. So far, the plasmonic properties of gold (Au) and silver (Ag) NPs have been widely exploited[3], but they are typically restricted to the infrared (IR) and visible regions[8]. In order to extend this range, other metals are required. Gallium nanoparticles (Ga NPs) are ideal candidates for achieving LSPR in the ultraviolet (UV) region thanks to its high bulk plasma energy (14 eV)[9]. Furthermore, varying their shape and size a wide spectral range from the IR to the UV can be obtained[10,11]. Ga NPs can be synthesized in a simple, fast and cost effective manner using thermal evaporation at low substrate temperature, which makes them compatible with many conductive and insulating substrates such as copper, quartz, glass, silicon (Si), plastics or sapphire and surfaces modified with 2D materials. Moreover, this bottom-up method is more suitable for large area applications than other physical techniques such as molecular beam epitaxy.

During deposition, liquid Ga forms truncated NPs due to the relaxation of its surface tension energy. As a consequence of this non-spherical shape there is a significant separation of the in-plane and out-of-plane resonances modes[10]. This fact is an advantage to other UV plasmonic material such as magnesium (Mg) and aluminium (Al) which do not show this geometry by self-assembly. Ga NPs merge during the growth due to coalescence or coarsening processes, sometimes ascribed to the Ostwald ripening mechanism[12]. As a result, for long times, a bimodal size distribution is obtained, with large NPs surrounded by smaller ones. Furthermore, Ga NPs have been ordered in arrays to create patterns[13].

When NPs are exposed to air, a 0.5-3 nm thick passivating layer of gallium oxide (Ga_2O_3) is formed preserving the liquid Ga from the environment. This shell keeps the

liquid Ga in a supercooled state[14]. Recently, Losurdo et al. demonstrated that Ga NPs can also exhibit small regions with solid γ-Ga phase when deposited on sapphire[15]. The formation of the Ga_2O_3 shell is therefore essential for the actual plasmonic response and stability of Ga NPs, but little attention has been paid to it so far.

Ga_2O_3 is a wide band gap semiconductor that has been mainly used as a transparent semiconducting oxide because of its low absorbance from the middle UV to the middle IR[16]. Its most stable crystalline phase is monoclinic β-Ga_2O_3, which has a low enthalpy of formation compared to other metal oxides (-1089.1 kJ/mol)[17], and requires a very low O_2 concentration to be formed due to the high solubility of O_2 in liquid Ga[18]. In the case of liquid Ga NPs, no crystalline phase has been detected for the native oxide layer, and the thickness of such layer is assumed to be self-limited by the attenuation of oxygen diffusion[19]. Despite the unintentional formation of the native oxide, the NPs have exhibited good properties for the enhancement of Raman scattering[20,21,22], for solid-liquid phase change memory elements[23], for waveguiding[5] and ellipsometric biosensing[24,25].

Most experimental studies have been focused on the modification of the LSPRs by adjusting the shape, size, and the substrate of these NPs[26]. Nevertheless, the control of the plasmonic properties of the Ga NPs through the thickness of the oxide shell is also an attractive approach, since it might be used to finely tune the intensity and wavelength of the resonance after the growth. Indeed, oxidation processes have been previously used for tuning the plasmonic resonance of Au NPs by controlling the thickness of an Al oxide mirror below them[27].

In this work, we have simulated the effect of the oxide shell thickness by means of discrete dipole approximation (DDA). Then, we performed oxidation experiments at different temperatures to induce the thickness variation and demonstrate that LSPR tuning can be achieved by this method. The stability of the NPs and the oxygen diffusion is investigated as well as the physical processes that govern the oxidation kinetics.

2. Experimental

Ga NPs are deposited by Joule-effect thermal evaporation using a vertical Edwards E306 system operating in high vacuum conditions (base pressure of 2×10^{-7} mbar). The size of the NPs depends on the total amount of Ga in the evaporation crucible. In order to

attain NPs with mean radius of about 60 nm, a fixed mass of 340 mg of Ga (99.9999% purity) was used. The evaporation process has been carried out under 50 W power, applied to a tungsten filament (99.90% purity). The working pressure during deposition was 1.5×10^{-5} mbar. Si (100) substrates were placed 200 mm away from the Ga source. The substrate holder is ice-cooled to avoid surface migration and coalescence of the droplets by unintentional heating.

Thermal treatments of the NPs were performed at atmospheric pressure in a horizontal quartz tube connected to a gas supply line with a QuadraTherm mass flow meter. The temperature inside the furnace is monitored by a proportional-integral-derivative controller. For the oxidation, a constant flow of 80 standard cubic centimetres (sccm) of 99.999% pure O_2 was used. Two series of samples were prepared. The first set was produced using a fixed annealing time of 15 minutes and varying the temperature (150, 200, 250, and 300 ºC). The second set was prepared under a fixed temperature of 300 ºC, but varying the time from 5 min to 1200 min. After the oxidation process, the samples were extracted from the tube, cooling down in ambient conditions. In addition, a reference β-Ga_2O_3 sample was prepared from 99.999% powder material and compacted under a compressive load to form a disk with a diameter of 7 mm and a thickness of 2 mm. It was then annealed in ambient air at 1200 °C for 3 h.

The optical properties of the samples were analysed by spectroscopic ellipsometry (SE), using a Jobin Yvon UVISEL system equipped with a Xe lamp (1.5-4.5 eV energy range), a 0º modulator and a 45º analyser. The measurements are taken in external reflection configuration at 70º incidence angle referred to the normal of the sample surface. The pseudo-dielectric constants of the material were obtained from the ellipsometric parameters psi (ψ) and delta (Δ)[28].

Scanning electron microscopy (SEM) was used to study the morphology of the Ga NPs. The microscope is a FEI XL30-SFEG system, operating with 10 keV electron beam and nominal lateral resolution of 4 nm, being the secondary electrons collected and analysed with an Everhart-Thornley detector.

The crystal structure of the samples has been analysed by grazing incidence X-ray diffraction (GIXRD) using a X'Pert Pro Panalytical system. The incident beam is produced in a Cu X-ray tube, focused by a Göbel mirror and collimated in a Soller slit (0.04 rad). The diffracted beam passes through a 0.18º parallel plate collimator, a graphite

(002) monochromator, and a Soller slit (0.04 rad) before being detected with a Xe gas scintillator. The incident angle was fixed at 0.5º and the 2θ angle was varied from 10º up to 90º, with a step of 0.04º and an acquisition time of 4 s per point.

X-ray photoelectron spectroscopy (XPS) has been used to characterize the chemical composition of Ga NPs deposited on Si wafer substrates. XPS spectra were acquired in an UHV chamber with a base pressure of 10^{-10} mbar equipped, a hemispherical electron energy analyser (SPECS Phoibos 150 spectrometer) and a 2-D delay-line detector, using a monochromatic Al-K_α (1486.74 eV) X-ray source. High resolution spectra were recorded at normal emission using an energy step of 0.025 eV and a pass-energy of 20 eV, which provide an overall instrumental peak broadening of 0.45 eV. The absolute binding energies of the photoelectron spectra were determined by referencing to the Si $2p_{3/2}$ transition at 99.0 eV. In order to compensate for the built up charge on the reference sample of Ga_2O_3, a flood gun (FG 15/40, SPECS) has been applied with low energy electrons of 2 eV and 2.12 μA. The spectra were analysed with the program CasaXPS[29] using a Shirley method for background subtraction.

In order to analyse the role of the oxide shell on the plasmonic properties of the Ga NPs, we evaluated the light-particle interaction with the DDA code DDSCAT 7.2[30]. Core-shell hemispheres were created by a target generation tool program executed by Matlab[31]. These targets were discretized into arrays of *N* polarizable points with polarizabilities α_i deployed on a cubic lattice at positions r_i. The points acquire dipole moments in response to the local electric field, which results from the incident electric field and the electric fields produced by the rest of dipoles. Thus, each dipole has a polarization $\vec{P_i}$ given by:

$$\vec{P_i} = \alpha_i \cdot \vec{E}(\vec{r_i}) \quad (1)$$

where $\vec{E}(\vec{r_i})$ is the electric field at $\vec{r_i}$ due to the sum of the incident wave and the contribution of each of the other *N-1* dipoles. The accuracy highly depends on the number of dipoles but very large values of *N* can make the DDA computationally prohibitive. Thus, a certain compromise is needed. Calculations of the absorption (Q_{abs}), scattering (Q_{scat}) and extinction (Q_{ext}) efficiency were carried out using a dipole lattice spacing of 2 nm to ensure a number of dipoles higher than 100000, achieving a good description of the target geometry by this method.

The error tolerance for convergence of the calculations was set to 10^{-5} at each wavelength[32]. The wavevector ($\vec{k}$) of the incident light was maintained parallel to the substrate (p polarization) in order to excite the out-of plane-mode of the NPs. The radius of the NP was maintained constant at 60 nm since this value is close to the average size obtained in the experiments. A Si substrate of 140×140×40 nm^3 was added below the Ga hemisphere. The input dielectric properties of liquid Ga and β-Ga_2O_3 were obtained from the literature[33,34]. The dielectric constants for Si were obtained from direct SE measurements of the (100) Si substrate used in the experiments.

3. Results and discussion

3.1 Discrete Dipole Approximation simulations

Prior to the experiment, calculations of the optical efficiencies were carried out for a hemisphere of liquid Ga on a Si substrate with a Ga_2O_3 shell of different thickness as described in the experimental part. If we assumed that there is no evaporation of Ga during the annealing treatment, the total amount of atomic Ga must be conserved in the structure and the different atomic densities of Ga and Ga_2O_3 must be considered.

The mean atomic density of liquid Ga[35] is $5.2 \cdot 10^{22}$ cm^{-3} while the atomic density of Ga in the oxide has been calculated to be $3.8 \cdot 10^{22}$ cm^{-3} from the volume and the number of atoms in a unit cell of β-Ga_2O_3[36]. The ratio between both densities is 1.37 which means that the transformation of liquid Ga to Ga_2O_3 would lead to a small increase of the total volume. The simulated structures have a liquid Ga core whose radius ranges from 60 nm down to 30 nm. On the other hand, the oxide shell increases from 0 to 30 nm keeping the total hemisphere radius constant at 60 nm. The expected volume increase due to the different atomic densities of Ga and Ga_2O_3 would lead to a radius increment of less than 10% in the worst case scenario. Therefore, for the sake of clarity, we neglected this difference in the atomic density between both materials in the simulations and maintain the hemisphere radius constant at 60 nm.

Regarding the simulations results, the analysis was focused on the Q_{ext} since it takes into account both scattering and absorption optical efficiencies and, considering that the ellipsometric system extracts the results from the reflected beam which suffers scattering

and absorption losses upon the reflection on the sample surface, the simulated Q_{ext} seems closer to the results obtained from SE. Later on, this argument is used later to compare the simulations with the SE measurements. The Q_{ext} is defined as the ratio between the nanoparticle cross-section and its geometrical cross-section. Figure 1(a) shows Q_{ext} as a function of the Ga_2O_3 shell thickness. As a reference, a pure Ga_2O_3 hemisphere on Si have also been simulated. The peak resonance is located around 270 nm (4.6 eV) for an unoxidized Ga NP and shifts to higher wavelengths when Ga_2O_3 thickness increases. This result is in agreement with previous works also based on the dipolar approximation theory[33]. The shift is a result of two combined factors: On one hand, the increase of the oxide shell produces a redshift due to the large difference between Ga and Ga_2O_3 dielectric constants[37]. On the other hand, the reduction of the Ga core shifts the resonance to shorter wavelengths. The overall redshift demonstrates that the effect of the oxide layer dominates the spectral behaviour of the resonance.

In order to verify the suitability of the simulated system we have performed test to analyse the effect of the substrate length, width and thickness, as well as the dipolar spacing. No shift higher than 1 nm is observed in the main peak at 270 nm due to any of these factors (graphs not shown). Minor changes were also detected in the shape and intensity of the peak around 400 nm but they do not affect the interpretation of our results since they are based on the shift of the resonance wavelength. Additionally, the role of the coupling and multiple scattering was studied as a function of the interparticle distance (5, 10 and 20 nm) for the unoxidized Ga NP close to another one of 20 and 60 nm radius. Again, no significant effects were detected in the wavelength of the peak (shifts lower than 2 nm), but mainly in the shape and intensity, which allows us neglecting the multiple scattering.

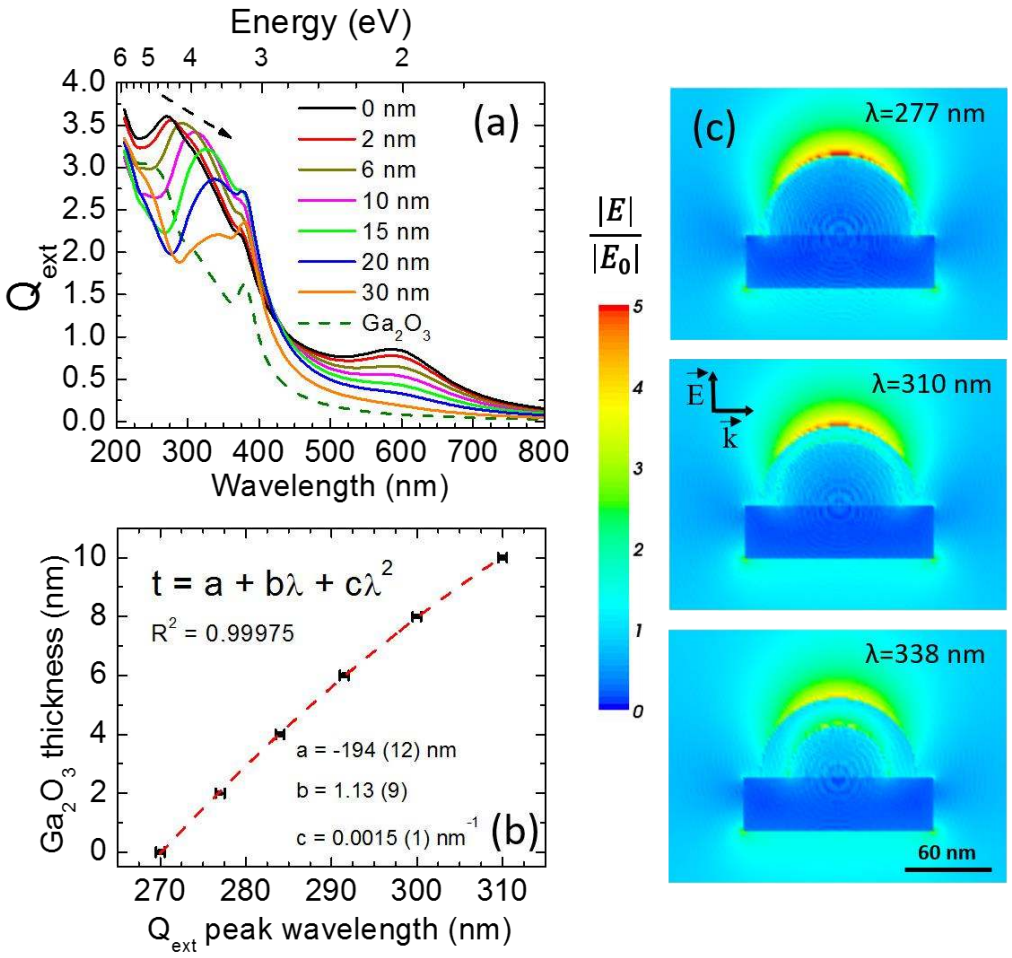

"**Figure 1.** (a) Simulated Q_{ext} of a core-shell hemispherical Ga NP on Si for different Ga_2O_3 shells thickness. A hemispherical Ga_2O_3 NP has also been simulated as a reference (b) Correlation between the Ga_2O_3 thickness and the maximum extinction wavelength and the corresponding fit. (c) Local electric field distribution for a core-shell NP with 2, 10 and 20 nm thick oxide shell. The wavelength in which the electric field has been evaluated is indicated in the figure and corresponds with the maximum Q_{ext}."

In addition to the red shift, the intensity of the maximum Q_{ext} also decreases with the increasing oxide thickness. As expected, the progressive inclusion of Ga_2O_3 reduces the plasmon resonance, which is hardly seen for thicknesses above 30 nm. The band around 600 nm also decreases, what suggests that it is due to high-order terms produced by phase retardation and substrate interactions[33].

In Figure 1(b), the oxide shell thickness is plotted versus the wavelength of the maximum plasmon resonance. The relationship between both parameters is fit with a

polynomial function. The fitting function is used later on to estimate the Ga_2O_3 thickness from the experimental wavelength shift obtained after annealing.

The simulations show that the plasmon wavelength can be significantly shifted even for small Ga_2O_3 thicknesses, e.g., the plasmon wavelength shifts 40 nm for 10 nm oxide shell. This shift is in the same order of magnitude than that obtained for Al NPs surrounded by Al_2O_3 layer[38]. For a Ag NP surrounded by a Ag_2O layer, for the same volume ratio between metal and oxide, a shift of about 25 nm is found[39]. What it is most remarkable is the effect in the plasmon intensity. While in our case only 5% of the plasmon intensity is reduced, in the Ag case it decreases by 40%. The explanation lies in the dielectric constants of the respective oxide. The extinction coefficient (k) of Ag_2O[40] is higher than that of Ga_2O_3, thus a higher attenuation of the resonance is expected due to dissipation of the evanescent waves of plasmons within the oxide shell. In comparison with other UV plasmonic materials such as Mg and Al, Ga has the strongest oxide sensitivity in terms of plasmon shifting[41]. Given these advantages, oxidation processes could offer a good strategy for tuning the plasmon resonance.

On the other hand, the effect of the oxidation in the near-field regime is studied. We have calculated the enhancement in the electric field in the vicinities of the hemisphere NP for three different thickness, 2, 10 and 20 nm thick (Figure 1(c)). The illuminating beam is a monochromatic linearly polarized plane wave with polarization ($\vec{E}$) and propagation ($\vec{k}$) direction indicated in the figure. The wavelength used for evaluating the near field is chosen to be that where the Q_{ext} is maximum, as indicated in the figure. The two lobules correspond to the electric dipolar resonance of the out-of-plane mode. Furthermore, it can be observed how the electric field is also enhanced in the metal-oxide interface aside from the air-oxide interface. Concerning the value of the enhancement in the legend, it is important to point it out that the hemisphere diameter strongly influences the maximum electric field enhancement. For Ga hemisphere NP this maximum is found for 80 nm of diameter[19]. Although, in comparison with other UV materials such as Mg and Al, Ga has the poorer plasmonic performance, its enhancement properties are less affected by its increasing oxide shell[42].

3.2 Effect of the thermal treatment

In order to corroborate the results obtained in the simulations, we performed thermal treatments to modify the oxide layer thickness of Ga NPs. The experiments, described in the experimental section, were carried out at different temperatures during 15 min. Figure 2(a) shows a typical SEM image of an as-deposited sample, which exhibits a bimodal distribution. The size histogram (Figure 2(e)) can be fit with two Gaussian functions centred at 25 and 276 nm, giving a mean radius of 60 nm.

These NPs do not evidence morphological changes at 150 ºC, as shown in Figure 2(b). However, when temperature increases a local plastic deformation is produced on the surface of the NPs (Figure 2(c) and (d)). If temperature increases up to 450 ºC (not shown), the Ga_2O_3 shell breaks, allowing some liquid Ga to leave the core. The breakdown is most likely due to the different pressures between inside and outside of the NPs.

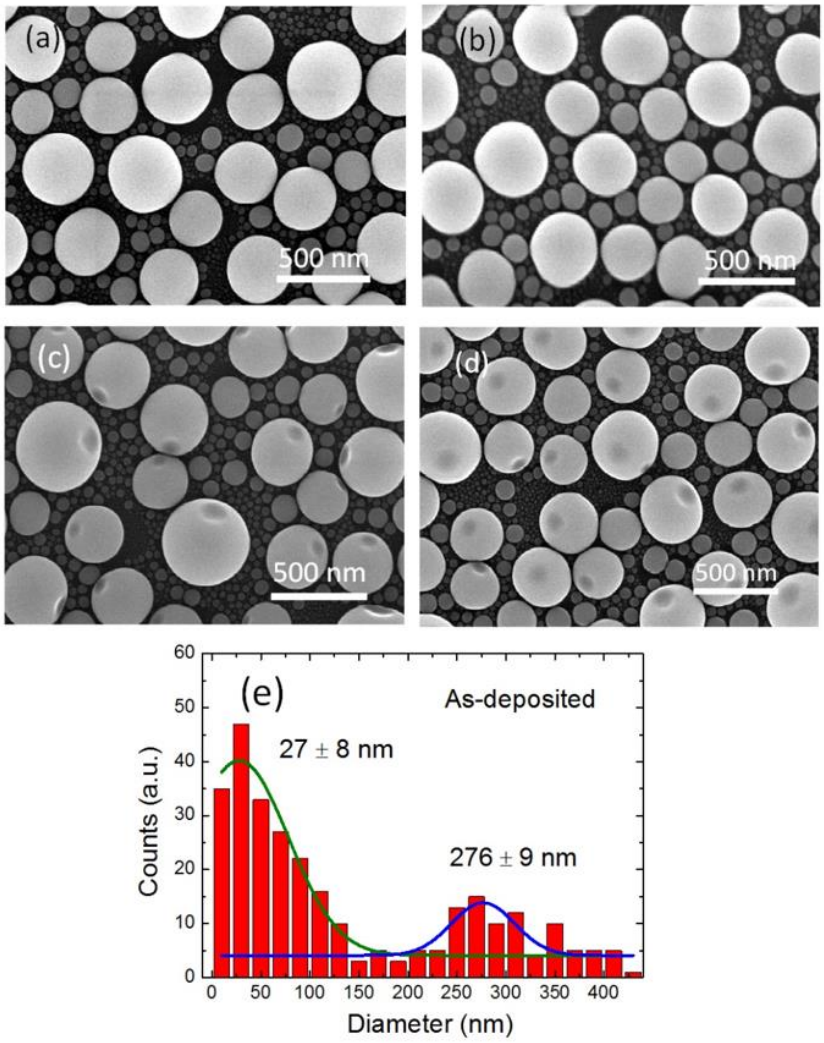

"**Figure 2.** SEM images of Ga NPs for different thermal treatments at 15 min. (a) As-deposited, (b) 150 ºC, (c) 250 ºC, and (d) 300 ºC. (e) Histogram of the size distribution for the as-deposited sample."

For tracking the extinction ascribed to the LSPR, we have measured the imaginary part of the pseudodielectric constant by SE measurements at a fixed angle of 70º, plotted in Figure 3. This incidence angle was chosen as it corresponds to the Brewster angle of the Si substrate. In this condition, the difference between the parallel and perpendicular reflection coefficients is maximized and the response of the system can be analysed more accurately[43]. The out-of-plane resonant mode is clearly visible for all the temperatures analysed. The in-plane mode lies in the infrared region, which is out of the spectral range of our experimental setup. The LSPR experiences a redshift as the annealing temperature increases (Figure 3(a)) as demonstrated in the previous simulations. For the sake of clarity, the shift has been plotted versus temperature in Figure 3(b). The progressive redshift is ascribed to the increasing oxide shell caused by oxygen diffusion. The obtained redshift from RT to 150 ºC is similar to that obtained by Wu *et al.* when Ga NPs are exposed to air after deposition, which is assumed to correspond to 0.5 to 2 nm oxide shell[10]. In our work, the oxide formation is studied at ambient pressure for temperatures lower than 300 ºC. At these conditions the oxygen diffusion is fostered by the different expansion coefficient of liquid Ga and Ga_2O_3. Indeed, that difference leads to the oxide shell breakdown at temperatures beyond 300 ºC. Since there is a two order of magnitude difference in the thermal expansion coefficient between liquid Ga and Ga_2O_3[44]. According to the formula $\Delta V/V_0=\alpha\cdot\Delta T$, a volume increase of 3.3% is expected for liquid Ga, with the expansion coefficient (α) equal to $1.2\cdot10^{-4}$ ºC^{-1}. In contrast, the change in the Ga_2O_3 shell is negligible (0.2%). This effect should increase the pressure inside the NP, promoting the oxygen diffusion and enlarging the Ga_2O_3 shell thickness. When the NP is cooled down to RT, the remaining liquid Ga relaxes reducing the pressure within the core. The pressure relief provokes the contraction of the oxide shell, which collapses inward. Thus, Figure 2(c) and 2(d) show clear evidences of the plastic deformation of the shell at room temperature.

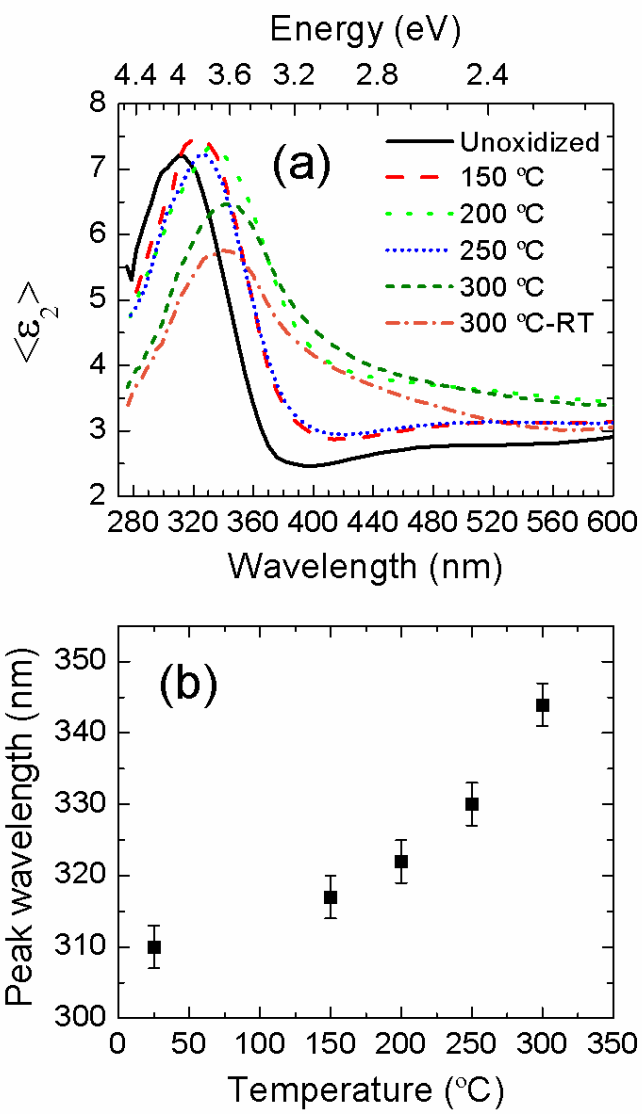

"**Figure 3.** (a) Imaginary part of the pseudodielectric constant obtained by SE measurements of samples oxidized at different temperatures compared to an unoxidized one kept at room temperature (RT) conditions. A sample oxidized at 300 ºC but cooled down slowly within the furnace is also included (300ºC-RT) (b) Peak plasmon wavelength corresponding to the maximum extinction as a function of the temperature."

In order to check the influence of the temperature decreasing ramp on the plastic deformation, a sample annealed at 300 ºC was cooled down within the furnace at a cooling rate below 1 ºC/min in order to reduce the thermal stress caused by a fast cooling. This sample shows the same red-shift ("Figure **3**(a)) as well as a higher attenuation of the plasmon resonance, likely due to the extra time exposed to intermediate temperatures until the furnace reaches RT. The most important characteristic of this sample, however,

is that most of the NPs do not show the local deformation in SEM characterization (image not shown). This proves that the local deformation is linked to the cooling rate, which plays an important role in the process. In our set-up, a cooling rate below 1 ºC/min guarantees the elastic recovery of the Ga_2O_3 shell, whereas a fast quenching at RT produces the plastic deformation.

XRD analysis was performed in order to investigate the crystallinity of the structures. Figure 4(a) shows the diffractogram of the as-deposited sample. The main feature of the graph is the two broad bands centred in ~35º and ~45º. These bands arise from the short range order of liquid Ga, as Yakema *et al.* reported[14]. Interestingly, this double band matches the δ-phase lines of solid Ga. Furthermore, liquid Ga has been discovered to be formed of dimeric molecules of Ga_2[35, 45] with a metal-covalent bond that could explain the origin of the ordering found in XRD. Moreover, layering of Ga atoms has been also demonstrated in a non-wetting substrate such as diamond[46].

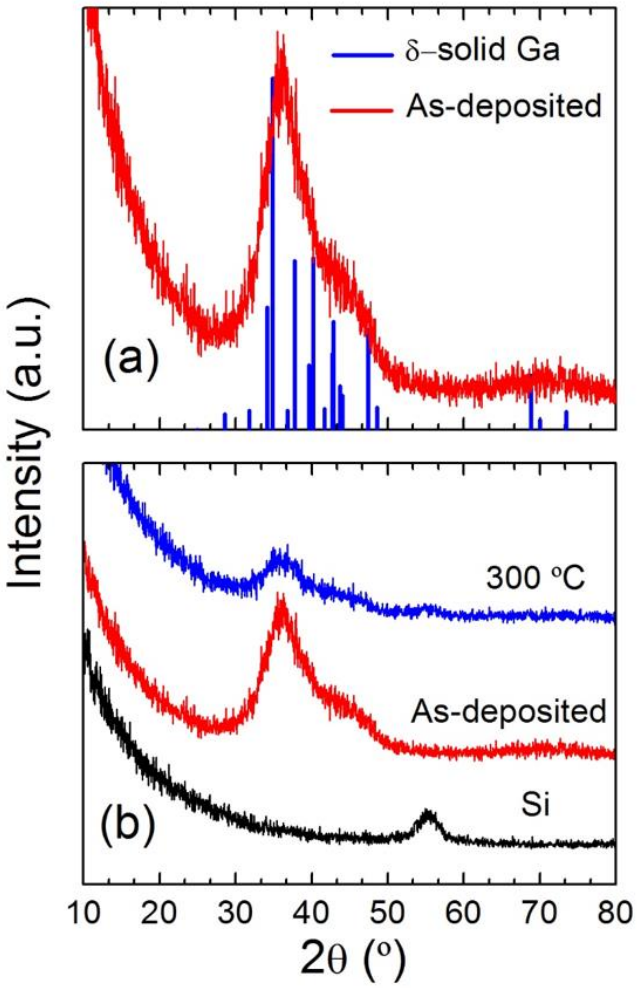

"**Figure 4.** (a) GIXRD measurements of as-deposited sample along with diffraction lines for δ-solid Ga (b) Comparison of the GIXRD patterns between as-deposited and 300 ºC oxidized sample. Data from Si substrate is also shown as reference."

Figure 4(b) shows the comparison between the XRD patterns of the as-deposited sample with the sample oxidized at 300 ºC and quenched rapidly to RT. In the XRD measurements, there are no significant differences between the sample cooled down rapidly to RT and the sample cooled down slowly at 1 ºC/min rate. The absence of sharp peaks reflects the amorphous character of the oxide layer in the thickness range under study. However, the band intensity associated to the liquid Ga attenuates with the increasing temperature, which points out the transformation of liquid Ga into Ga_2O_3 inside the NP. This result, together with the SE redshift and the DDA simulations, indicate the increasing thickness of the oxide shell.

Another important factor in this oxidation process is the annealing time. A set of samples was produced by oxidation at different times, from 5 min up to 1200 min. The temperature was fixed to 300 ºC, since this is the highest limit prior to the breakdown of the NPs. Figure 5(a) shows the pseudodielectric function for such set obtained by SE. The plasmon resonance red-shifts when time is increased, being the results plotted in Figure 5(b). A clear saturation is observed for the wavelength of the LSPR, while the intensity decreases with time. This shift is interpreted, again, as an increasing Ga_2O_3 shell; the behaviour shown in Figure 5(b) is representative for bulk or thin film systems that are oxidized by diffusion[47]. Moreover, the growth of the oxide depends on other parameters such as temperature, pressure, electric field, diffusion coefficients, oxygen activity, etc.[48]

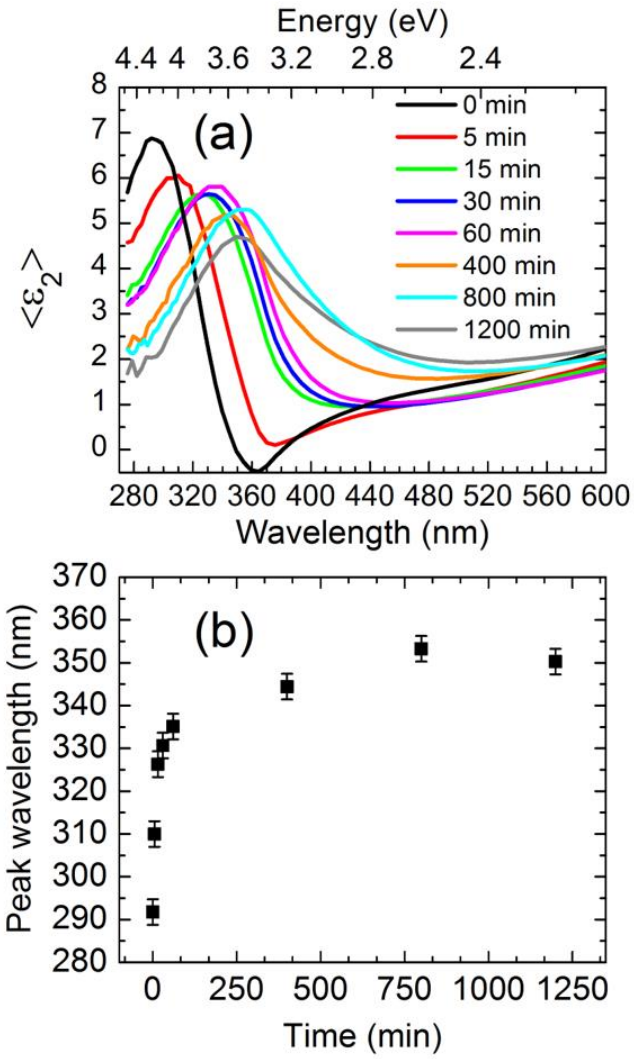

"**Figure 5.** (a) Imaginary part of pseudodielectric constant obtained by SE measurements of samples oxidized at different times. (b) Peak plasmon wavelength corresponding to the maximum extinction as a function of the annealing time."

In order to confirm the increase of the Ga_2O_3 layer in more detail, *ex-situ* XPS measurements were performed after the annealing. In the survey scan (not shown) Ga 2p, 3s, 3p, and 3d, electronic levels can be observed. For a chemical analysis, the 3d level was selected because of its low binding energy value that corresponds to a higher sampling depth.

Figure 6 (a) and (b) show XPS spectra of the samples for both the temperature and time series, respectively. The two main Ga-3d peaks, with binding energies (BE) centered at 18.7 eV and 21.3 eV are distinguishable in both series. These peaks correspond to emission from Ga atoms in different chemical environments, metallic and oxide,

respectively, in good agreement with the literature[49,50]. Thanks to the fine energy step used (0.025 eV) it is possible to resolve the 3d doublet of the metallic Ga.

As temperature or time increases, the signal from the metallic Ga decreases as a consequence of the oxidation. The 3d doublet progressively disappears with the increasing temperature (Figure 6(a)), revealing the increasing thickness of the oxide shell and in agreement with the data obtained by XRD and SE. This behaviour also occurs in the time series, where the metallic 3d doublet is completely vanished. A quantitative analysis of the ratio between the metallic Ga and the oxide peaks area has been carried out and it is shown in the inset of Figure 6(b). A dash-line has been plotted as a guide to the eye. The Ga metallic doublet has been fit with two Gaussian-Lorentzian mixed functions centred at 18.4 ± 0.1 and 18.9 ± 0.1 eV, that match the ratio between both intensities[51,52]. The sum of these two areas has been divided by the area coming from the rest of contributions due to oxidized peaks. The trend in Figure 6 (b) resembles that of the Figure 5 (b), indicating the same physical origin, i.e., the increasing thickness of the oxide shell. The possibility of Ga diffusion through Si has been dismissed because of the low temperatures and the low diffusivities[53].

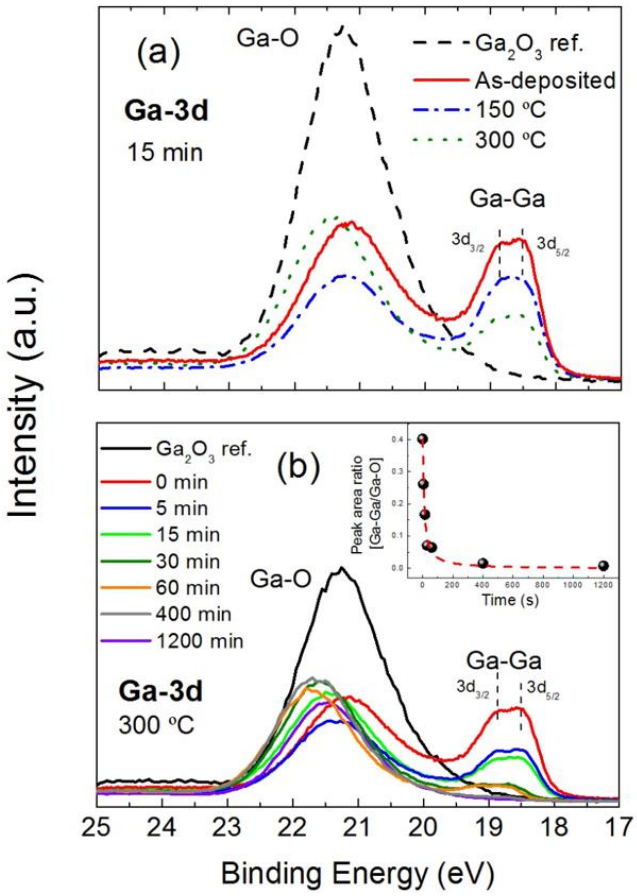

"**Figure 6.** (a) XPS spectra of the 3d level of Ga for samples oxidized at different temperatures for 15 min and (b) samples oxidized for different times at 300 ºC. The data for the as-deposited sample and a bulk Ga_2O_3 reference sample are also included. The inset corresponds to the quantitative analysis of the ratio between the metallic Ga and the oxide peaks area."

The sample oxidized at 300 ºC during 1200 min does not show any signal from metallic Ga due to the probing depth of the technique for this 3d level that is limited to 8-10 nm[50]. However, this sample still shows a clear plasmon resonance in Figure 5 (a). This fact is very important because it allows us estimating the thickness of the oxide shell. The lack of the metallic Ga signal means that there are no electrons coming from metallic Ga because the Ga_2O_3 thickness is at least equal to the escape depth of the electrons at this binding energy. Nearly all electrons (>95%) come from a depth that is three times the distance of the inelastic mean free path, equal to ≈3 nm for the kinetic energy of the Ga 3d level. Consequently, the thickness of the oxide shell in this sample is at least 9 nm.

The analysis of the high binding energy 2p level (not shown) has a similar behaviour than the 3d level; the signal from metallic Ga disappear when time and temperature

increase. However, the sample oxidized at 300 ºC during 30 min does not show any metallic Ga signal because of the higher surface sensitivity of this level. Indeed, according to the energy of the electrons emitted from the Ga 2p level, the associated probing depth is 4 nm approximately. Then, the oxide thickness for 30 min of oxidation should be higher than 4 nm.

We have clearly established that the LSPR of Ga NPs can be tuned by thermal treatments thanks to the oxygen diffusion and the formation of a thicker Ga_2O_3 shell. Now, we can model the mechanism that govern this process. For that, we assume the polynomial law presented in Figure 1 (b), which accounts for the plasmon shift expected from the oxide growth. Thus, we have substituted the shift found in the SE measurements for oxidations at different times with the oxide thickness in nm obtained from that law. Since the simulation limitations make difficult to match the maxima of the experimental and the simulated spectra, we used the shift instead for monitoring the oxide growth. This approach has been also used in Ag_2O films, where the surface plasmon resonance was studied using the optical reflectivity[54]. In our case, we use this dependence to estimate the experimental oxide thickness from the SE data for both the temperature and time series. Although the peak wavelength does not shift equally for the different NP sizes, the error that, according to our DDA simulations, one assumes in the oxide thickness determination is about ±20% for NPs with radius between 30 and 60 nm. We believe that this error is reasonable to justify the use of the shift although a more accurately analysis would require higher size uniformity in the NP array.

The obtained results are shown in Figure 7 (a) and (b) for both the temperature and the time series, respectively. For the temperature series, the estimated thickness increases following a non-linear function. Since the time was kept constant in this series, the thickness will follow the same function as the reaction rate constant with temperature. This function follows an Arrhenius-like behaviour, which is indicated in Figure 7(a) as a guide to the eye. Clearly, this trend suggests that the process is thermally activated. Thereupon, an inset with the Arrenhius plot is shown in Fig. 7 (a). The activation energy from the fitting is equal to183.7 meV. This low value is likely due to the high diffusivity of the oxygen ions in Ga_2O_3[18].

For the time series, the Ga_2O_3 thickness is plotted as a function of time in Figure 7(b) at an oxidation temperature of 300 ºC. The quantitative XPS analysis displayed in the

inset of Figure 6(b) follows a similar behaviour, and the value of the Ga_2O_3 thickness fully agrees with the estimation provided by XPS results.

The most general models describing the oxidation of metals with time are linear, parabolic, cubic and logarithm well described in the general theory explained by Cabrera and Mott (CM)[55]. The linear model describes well ultralight metals, such as potassium and sodium, that forms porous and non-protective oxides. The parabolic (also known as Tammann-Pilling-Bedworth law)[56] and cubic models are most commonly observed in heavy metals such as iron, copper and nickel at high temperature regimes[57]. This model is based on the diffusion of ions through the oxide. On the other hand, the logarithm model only occurs at relatively low temperatures. It was discovered by Evans[58] and properly explained by Uhlig[59] some years later. This law also governs low temperature oxidation of heavy metals such as iron[45], zinc[60] and titanium[61]. It is based on the formation of a space charge layer due to the equalizing of the Fermi levels of the metal and the semiconducting oxide at the junction.

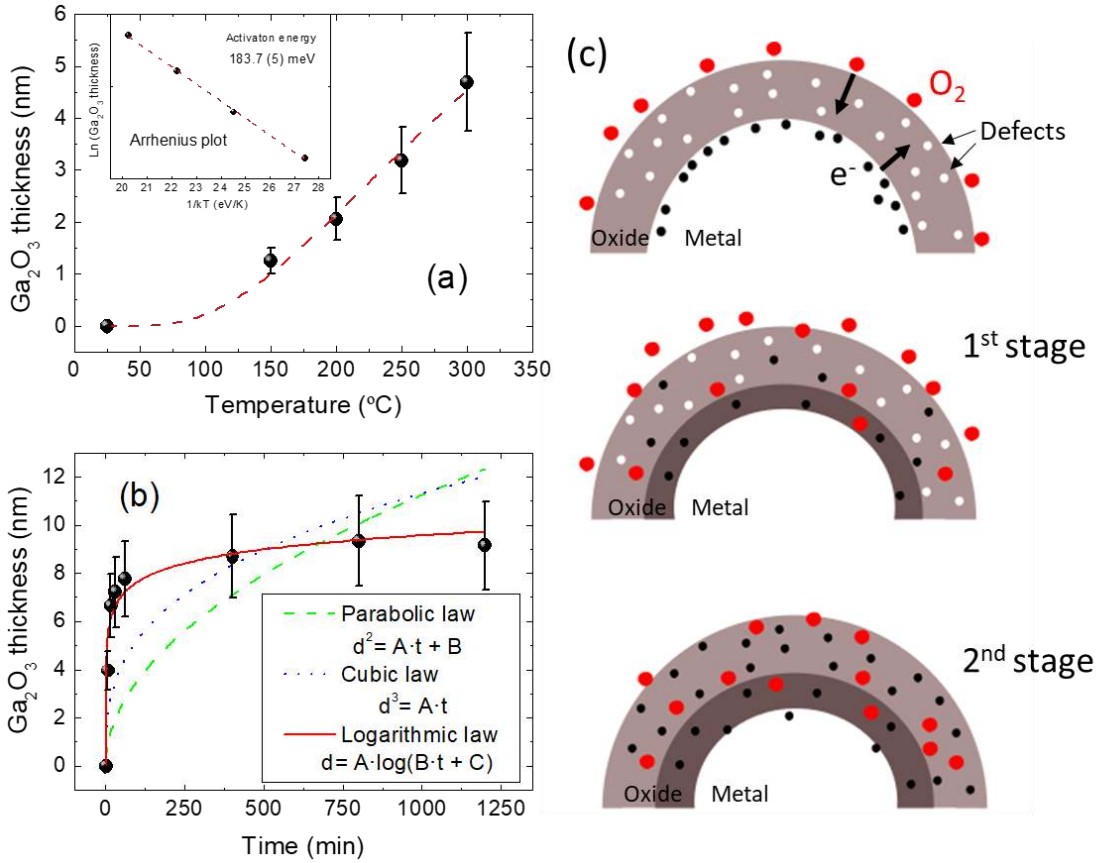

"**Figure 7.** Estimated Ga_2O_3 thickness obtained from the application of DDA fit to SE data for the (a) temperature and (b) time series. A guide to the eye has been plotted in (a). The inset corresponds to the Arrenhius plot. Parabolic, cubic and logarithmic equations have been fitted to the data points in (b). (c) Sketch of the oxidation mechanism for the logarithmic model."

We have carried out fittings of our results with the parabolic, cubic and logarithmic models (Figure 7(b)). The logarithm model (solid line) shows the best agreement with the experimental data. The two stages presented in the Figure 7(b) corresponds with the formation of two kinds of space charge according to Uhlig' model. In the first stage, where oxidation rate is very fast, the space charge consists of electrons trapped at the available imperfection or impurity sites in the oxide. In the second stage, the space charge has a decreasing fraction of the available sites exhibiting charge as the oxide thickens. We have exemplarily sketched the mechanism in Figure 7(c). The start point is a metallic Ga full of electrons (black circles) below a native oxide with imperfection or defects (white circles). In the first stage electrons from Ga moves through vacancies of the oxide until they reach the oxide-air interface and ionize oxygen atoms (red circles). These ions diffuse through the oxide until the reach the oxide-metal interface and react with the Ga atoms of the metal. In the second stage, although, the mechanism does not change, the rate falls with time.

It is worth mentioning that the logarithmic model was developed for thin films and bulk materials and not for nanomaterials. In those cases, size effects are obviously expected. Although, there are some experimental studies of oxidation of NPs, nowadays there is not a general theory to extrapolate the oxidations kinetics that takes place in bulk materials to their nanosize counterparts. The main cause is the lack of constants and parameters that could intensely change with the diameter of the NPs such as: activation energies, diffusion constants, lattice parameters, work functions etc.

Nevertheless, the basic arguments used to explain the logarithmic growth of the oxide layer in a thin film seems valid for a nanostructure. They can be explained with the CM theory that include the logarithmic model[62]. Up to our knowledge, there is no conclusive studies about the oxidation kinetics of Ga thin films within the framework of the CM theory. We hypothesize that a nanoparticle may have more resistance to oxidation than a thin film due to the reduction of defects but further investigations would be necessary to compare both scenarios.

According to our data, the model that best matches the oxide thickness growth as a function of the oxidation time is the logarithmic model. This law allows us to accurately control the maximum plasmon resonance wavelength in some dozens of nm.

4. Conclusions

We have studied the effect of the variation of the Ga_2O_3 shell thickness on the plasmonic properties of the Ga NPs via DDA simulations. The maximum plasmon resonance wavelength redshifts several nm with a small decrease in the intensity of the Q_{ext}. Experiments have been carried out to confirm those results by means of thermal treatments varying both the temperature and the annealing time. SE has been used to determine the wavelength of the LSPR of the out-of-plane mode. The increase of the Ga_2O_3 thickness has been demonstrated by XPS measurements. Both methods show that the metallic core of the Ga NPs reduces with the increasing temperature and time. We have estimated the thickness of the Ga_2O_3 after the oxidation processes by using the simulations and the experimental data. Furthermore, we have investigated the mechanisms involved in the oxidation rate with time, which follows a logarithmic model. This study opens the possibility of tuning the LSPR of Ga NPs in the UV range by oxidation processes at low temperatures without affecting the near and far-field plasmonic response significantly.

Acknowledgments

We thank Eduardo Ruiz for technical help during the sample preparation. We also thank Dr. Emilio Nogales and Dr. Bianchi Méndez for providing the Ga_2O_3 reference sample and for fruitful discussions. This research is supported by the MINECO (CTQ2014-53334-C2-2-R and MAT2016-80394-R) and Comunidad de Madrid (NANOAVANSENS ref. S2013/MIT-3029) projects. ARC acknowledges Ramón y Cajal program (under contract number RYC-2015-18047). FN acknowledges support from Marie Sklodowska-Curie grant agreement No 641899 from the European Union's Horizon 2020 research and innovation programme.

References

1. Stockman, M. I. 2011 Nanoplasmonics: past, present, and glimpse into future *Opt. Express* ***19*** 22 22029-22106.

2. Anker, J. N.; Hall, W. P.; Lyandres, O.; Shah, N. C.; Zhao, J.; Van Duyne, R. P. 2008 Biosensing with plasmonic nanosensors *Nat. Mater.* ***7*** 6 442-453.

3. Willets, K. A.; Duyne, R. P. V. 2007 Localized surface plasmon resonance spectroscopy and sensing *Annu. Rev. Phys. Chem.* ***58*** 1 267-297.

4. Oulton, R. F.; Sorger, V. J.; Genov, D. A.; Pile, D. F. P.; Zhang, X. 2008 A hybrid plasmonic waveguide for subwavelength confinement and long-range propagation *Nat. Photon.* ***2*** 8 496-500.

5. Krasavin, A. V.; Zheludev, N. I. 2004 Active plasmonics: Controlling signals in Au/Ga waveguide using nanoscale structural transformations *Appl. Phys. Lett.* ***84*** 8 1416-1418.

6. Jeon, T. Y.; Kim, D. J.; Park, S.-G.; Kim, S.-H.; Kim, D. H. 2016 Nanostructured plasmonic substrates for use as SERS sensors *Nano Convergence* ***3*** 1 18.

7. Butun, S.; Tongay, S.; Aydin, K. 2015 Enhanced light emission from large-area monolayer MoS_2 using plasmonic nanodisc arrays *Nano Lett.* ***15*** 4 2700-2704.

8. Hubenthal, F.; Ziegler, T.; Hendrich, C.; Alschinger, M.; Träger, F. 2005 Tuning the surface plasmon resonance by preparation of gold-core/silver-shell and alloy nanoparticles *Eur. Phys. J. D - Atomic, Molecular, Optical and Plasma Physics* ***34*** 1 165-168.

9. Hunderi, O.; Ryberg, R. 1974 Band structure and optical properties of gallium *J. Phys. F: Metal Physics* ***4*** 11 2084.

10. Wu, P. C.; Kim, T.-H.; Brown, A. S.; Losurdo, M.; Bruno, G.; Everitt, H. O. 2007 Real-time plasmon resonance tuning of liquid Ga nanoparticles by in situ spectroscopic ellipsometry *Appl. Phys. Lett.* ***90*** 10 103119.

11. Kang, M. Formation and properties of metallic nanoparticles on compound semiconductor surfaces *PhD Thesis* University of Michigan, 2014.

12. Woorhees, P. W. 1985 Theory of Ostwald Ripening *J. Stat. Phys.* ***38***.

13. Bollani, M.; Bietti, S.; Frigeri, C.; Chrastina, D.; Reyes, K.; Smereka, P.; Millunchick, J. M.; Vanacore, G. M.; Burghammer, M.; Tagliaferri, A.; Sanguinetti, S. 2014 Ordered arrays of embedded Ga nanoparticles on patterned silicon substrates *Nanotechnology* ***25*** 20 205301.

14. Yarema, M.; Wörle, M.; Rossell, M. D.; Erni, R.; Caputo, R.; Protesescu, L.; Kravchyk, K. V.; Dirin, D. N.; Lienau, K.; von Rohr, F.; Schilling, A.; Nachtegaal, M.; Kovalenko, M. V. 2014 Monodisperse colloidal gallium nanoparticles: synthesis, low temperature crystallization, surface plasmon resonance and li-ion storage *J. Am. Chem. Soc.* ***136*** 35 12422-12430.

15. Losurdo, M.; Suvorova, A.; Rubanov, S.; Hingerl, K.; Brown, A. S. 2016 Thermally stable coexistence of liquid and solid phases in gallium nanoparticles *Nat. Mater.* ***15*** 9 995-1002.

16. S. I. Stepanov, V. I. N., V. E. Bougrov, and A. E. Romanov 2016 Gallium oxide: properties and applications - a review *Rev. Adv. Mater. Sci.* ***44*** 1 63-86.

17. Group, T. a. F., *Handbook of chemistry and Physics*. 93rd ed.; CRC: 2013.

18. Zinkevich, M.; Aldinger, F. 2004 Thermodynamic assessment of the gallium-oxygen system *J. Am. Ceram. Soc.* ***87*** 4 683-691.

19. Sanz, J. M.; Ortiz, D.; Alcaraz de la Osa, R.; Saiz, J. M.; González, F.; Brown, A. S.; Losurdo, M.; Everitt, H. O.; Moreno, F. 2013 UV plasmonic behavior of various metal nanoparticles in the near- and far-field regimes: geometry and substrate effects *The J. Phys. Chem. C* ***117*** 38 19606-19615.

20. Yang, Y.; Callahan, J. M.; Kim, T.-H.; Brown, A. S.; Everitt, H. O. 2013 Ultraviolet Nanoplasmonics: A demonstration of surface-enhanced raman spectroscopy, fluorescence, and photodegradation using gallium nanoparticles *Nano Lett.* ***13*** 6 2837-2841.

21. Wu, P. C.; Khoury, C. G.; Kim, T.-H.; Yang, Y.; Losurdo, M.; Bianco, G. V.; Vo-Dinh, T.; Brown, A. S.; Everitt, H. O. 2009 Demonstration of surface-enhanced raman scattering by tunable, plasmonic gallium nanoparticles *J. Am. Chem. Soc.* ***131*** 34 12032-12033.

22. Pau, J. L.; García-Marín, A.; Hernández, M. J.; Lorenzo, E.; Piqueras, J. 2016 Optical biosensing platforms based on Ga–graphene plasmonic structures on Cu, quartz and SiO2/Si substrates *Phys. Status Solidi (b)* ***253*** 4 664-670.

23. Soares B. F. , J. F. a. Z. N. I. 2007 All-optical phase-change memory in a single gallium nanoparticle *Phys. Rev. Lett.* ***98***.

24. García Marín, A.; Hernández, M. J.; Ruiz, E.; Abad, J. M.; Lorenzo, E.; Piqueras, J.; Pau, J. L. 2015 Immunosensing platform based on gallium nanoparticle arrays on silicon substrates *Biosens. Bioelectron.* ***74*** 1069-1075.

25. Antonio García Marín, T. G.-M., Cristina Navio Bernabeu, María Jesús Hernández, Juan Piqueras, Jose Luis Pau, Félix Parienteb, and Encarnación Lorenzo 2016 Gallium plasmonic nanoparticles for label-free DNA and single nucleotide polymorphism sensing *Nanoscale* ***8*** 18 9842-9851.

26. Albella, P.; Garcia-Cueto, B.; González, F.; Moreno, F.; Wu, P. C.; Kim, T.-H.; Brown, A.; Yang, Y.; Everitt, H. O.; Videen, G. 2011 Shape matters: plasmonic nanoparticle shape enhances interaction with dielectric substrate *Nano Lett.* ***11*** 9 3531-3537.

27. Ding, T.; Sigle, D.; Zhang, L.; Mertens, J.; de Nijs, B.; Baumberg, J. 2015 Controllable tuning plasmonic coupling with nanoscale oxidation *ACS Nano* ***9*** 6 6110-6118.

28. Tompkins, H. G., Chapter 1 - Theoretical Aspects. In a user's guide to ellipsometry, Academic Press: San Diego, 1993; pp 1-18.

29. Fairley, N. 2006 CASAXPS: Spectrum processing software for XPS, AES and SIMS (Version 2. 3. 14) *CASA Software Ltd.*

30. Draine, B. T.; Flatau, P. J. 1994 Discrete-Dipole approximation for scattering calculations *J. Opt. Soc. Am. A* ***11*** 4 1491-1499.

31. John Feser, A. N. S. DDSCAT convert: a target generation tool, https://nanohub.org/resources/ddaconvert.

32. Draine, B. T. F., Piotr J. User guide for the discrete dipole approximation code DDSCAT 7.2.

33. Knight, M. W.; Coenen, T.; Yang, Y.; Brenny, B. J. M.; Losurdo, M.; Brown, A. S.; Everitt, H. O.; Polman, A. 2015 Gallium plasmonics: deep subwavelength spectroscopic imaging of single and interacting gallium nanoparticles *ACS Nano* ***9*** 2 2049-2060.

34. Al-Kuhaili, M. F.; Durrani, S. M. A.; Khawaja, E. E. 2003 Optical properties of gallium oxide films deposited by electron-beam evaporation *Appl. Phys. Lett.* ***83*** 22 4533-4535.

35. Hoyer, W.; Thomas, E.; Wobst, M. 1980 Structure investigation on liquid gallium *Kristall und Technik* ***15*** 8 903-910.

36. Li. Liandi, Wei Wei, M. Behrens 2012 Synthesis and characterization of α-, β-, and γ-Ga_2o_3 prepared from aqueous solutions by controlled precipitation *Solid State Sci. 14* 7 971-981.

37. García, M. A. 2012 Surface plasmons in metallic nanoparticles: fundamentals and applications *J. Appl. Phys.* ***45*** 38.

38. Ziashahabi, A.; Poursalehi, R. 2015 The effects of surface oxidation and interparticle coupling on surface plasmon resonance properties of aluminum nanoparticles as a UV plasmonic material *Proc. Mat. Sci.* ***11*** 434-437.

39. Kuzma, A.; Weis, M.; Flickyngerova, S.; Jakabovic, J.; Satka, A.; Dobrocka, E.; Chlpik, J.; Cirak, J.; Donoval, M.; Telek, P.; Uherek, F.; Donoval, D. 2012 Influence of surface oxidation on plasmon resonance in monolayer of gold and silver nanoparticles *J. Appl. Phys.* ***112*** 10 103531.

40. Pettersson, L. A. A.; Snyder, P. G. 1995 Preparation and characterization of oxidized silver thin films *Thin Solid Films* ***270*** 1 69-72.

41. Moreno, F.; Albella, P.; Nieto-Vesperinas, M. 2013 Analysis of the spectral behavior of localized plasmon resonances in the near- and far-field regimes *Langmuir* ***29*** 22 6715-6721.

42. Gutierrez, Y.; Ortiz, D.; Sanz, J. M.; Saiz, J. M.; Gonzalez, F.; Everitt, H. O.; Moreno, F. 2016 How an oxide shell affects the ultraviolet plasmonic behavior of Ga, Mg, and Al nanostructures *Opt. Express* ***24*** 18 20621-20631.

43. Verre, R.; Fleischer, K.; Smith, C.; McAlinden, N.; McGilp, J. F.; Shvets, I. V. 2011 Probing the out-of-plane optical response of plasmonic nanostructures using spectroscopic ellipsometry *Phys. Rev. B* ***84*** 8 085440.

44. Hai Yoon Park, M. S. J. 1982 Thermodynamic and Transport Properties of Liquid Gallium *J. Korean Nuc. Soc.* ***14*** 1

45. Ghigna, P.; Spinolo, G.; Parravicini, G. B.; Stella, A.; Migliori, A.; Kofman, R. 2007 Metallic versus covalent bonding: Ga nanoparticles as a case study *J. Am. Chem. Soc.* ***129*** 25 8026-8033.

46. Huisman, W. J.; Peters, J. F.; Zwanenburg, M. J.; de Vries, S. A.; Derry, T. E.; Abernathy, D.; van der Veen, J. F. 1997 Layering of a liquid metal in contact with a hard wall *Nature* ***390*** 6658 379-381.

47. Holland, L., Vacuum Deposition of Thin Films. Chapman and Hall Ltd.: 11 New ftter Lane, London, 1970.

48. Fromhold, A. T., Theory of Metal Oxidation. North Holland Publishing Company: Amsterdam, 1976; Vol. 1.

49. Carli, R.; Bianchi, C. L. 1994 XPS analysis of gallium oxides *Appl. Surf. Sci.* ***74*** 1 99-102.

50. Surdu-Bob, C. C.; Saied, S. O.; Sullivan, J. L. 2001 An X-ray photoelectron spectroscopy study of the oxides of GaAs *Appl. Surf. Sci.* ***183*** 1–2 126-136.

51. Higashiyama, K.; Kono, S.; Kinoshita, T.; Miyahara, T.; Kato, H.; Ohsawa, H.; Enta, Y.; Maeda, F.; Yaegashi, Y. 1987 Surface core-level shifts of the Si(111)√3 × √3-Ga surface *Surf. Sci. Lett.* ***186*** 3 568-574.

52. Dürrwächter, M.; Indlekofer, G.; Boyen, H. G.; Oelhafen, P.; Quitmann, D. 1993 Core level binding energy shifts in liquid binary alloys: Au-Ga *J. of Non-Crystalline Solids* ***156*** 241-245.

53. DeVries, D. L. K. a. D. B. 1969 Diffusion in silicon *J. Electrochem. Soc.* 358-421.

54. Jesica, M. J. S.; Lucía, B. S.; Daniel, C. S.; Fabián, A. V. 2010 Determination of nanometric Ag_2O film thickness by surface plasmon resonance and optical waveguide mode coupling techniques *J. Optics* ***12*** 4 045002.

55. Mott, N. C. a. N. F. 1949 Theory of the oxidation of metals *Rep. Prog. Phys.* ***12*** 163.

56. N. B. Pilling, R. E. B. 1923 The oxidation of metals at high temperatures *J. Inst. Met.* ***29*** 529-591.

57. Morris, L. A. The oxidation properties of iron-nickel alloys in carbon dioxide-carbon monoxide atmospheres at 1000ºC. McMaster University, 1965.

58. Evans, U. R. 1946 Recent work on corrosion and oxidation *J. Chem. Soc.* 207-214.

59. Uhlig, H. H. 1956 Initial oxidation rate of metals and the logarithmic equation *Acta Metallurgica* ***4*** 5 541-554.

60. Uhlig, V. O. N. a. H. H. 1965 Logarithmic oxidation kinetics of zinc *J. Electrochem. Soc.* ***112*** 12 1181-1185.

61. Waber, J. T.; Sturdy, G. E.; Wise, E. N. 1953 The logarithmic growth law for the oxidation of titanium *J. Am. Chem. Soc.* ***75*** 9 2269-2270.

62. Chernavskii, P. A.; Peskov, N. V.; Mugtasimov, A. V.; Lunin, V. V. 2007 Oxidation of metal nanoparticles: Experiment and model *Russian J. Phys. Chem. B* **1** 4 394-411.